# *In situ* structure of bacterial 50S ribosomes at 2.98 Å resolution from vitreous sections.

Ashraf Al-Amoudi[1*#], Rozbeh Baradaran[2,3*], Xukun Yuan[2], Andreas Naschberger[2#]

[1] Electron Microscopy Lab, Imaging and Characterization Core Labs, King Abdullah University of Science and Technology (KAUST), 23955 Thuwal, SA

[2] King Abdullah University of Science and Technology (KAUST), Biological and Environmental Science and Engineering Division, 23955 Thuwal, SA

[3] Structural Biology STP, The Francis Crick Institute, 1 Midland Road, London NW1 1AT, UK

* These authors contributed equally to this work

# Correspondence to: ashraf.alamoudi@kaust.edu.sa and andreas.naschberger@kaust.edu.sa

**Abstract:**

*In situ* high-resolution structure determination is limited to samples that are thin enough to be penetrated by the electron beam during imaging. Currently, the most widely used method for sample thinning involves focused ion or plasma beam milling of biological specimens to produce lamellae with thicknesses as low as 100–150 nm. However, surface damage caused by the milling process can extend 30–60 nm deep, leaving only a narrow undamaged core and thereby restricting the usable lamella thickness. This imposes significant limitations on single-particle analysis of smaller macromolecular complexes due to elevated structural noise, which cannot be avoided *in situ* because of the dense cellular environment composed of proteins, membranes, and other ultrastructures. Therefore, alternative methods capable of producing thinner samples are needed to reduce this structural background and enable *in situ* single-particle analysis. Here, we demonstrate that high-resolution structures at side-chain level can be obtained from vitreous sections prepared by cryo-ultramicrotomy, both *in vitro* and *in situ*. We optimized the method to produce high-quality sections as thin as 30–50 nm, free from significant surface damage such as crevasses. Using this approach, we determined the structure of the 50S ribosomal subunit *in vitro* in a standard buffer system and show that orientation bias can be overcome in using this technique. In addition, we systematically analyzed section thickness and show that our ultrathin sections are thin enough to physically cleave 70S ribosomes, suggesting that this approach may be particularly well suited for the structural analysis of smaller macromolecules. Finally, we present a sub-3 Å resolution reconstruction of the 50S ribosomal large subunit *in situ* from bacterial cells. Future directions and potential applications are discussed, with a focus on advancing *in situ* single-particle analysis of smaller macromolecular complexes.

**Introduction:**

*In situ* cryo-electron microscopy (cryo-EM) enables the high-resolution structural determination of macromolecular targets in their near-native, hydrated state, embedded within the preserved cellular ultrastructure [1]. Typically using Cryo-Electron Tomography (cryo-ET), cryo-fixed cells or tissues are imaged by acquiring multiple tilt series, which are subsequently computationally aligned and processed to generate tomograms. These tomograms are representing localized reconstructed volumes corresponding to a portion of a cell [2]. Using subtomogram averaging, the particles of interest within the volume are localized and extracted as subvolumes, which can then be aligned and averaged to obtain high-resolution reconstructions *in situ*. [3-5]. However, due to the crowded cellular environment and the poor contrast and signal-to-noise ratio (SNR) caused by relatively thick samples and structured background noise, high-resolution *in situ* structures are currently restricted mainly to large molecular assemblies, such as ribosomes [6].

More recently, it has been demonstrated that *in situ* cryo-EM is not limited to tomography alone but also *in situ* single-particle analysis (SPA) is applicable on cellular lamellas [7-9]. This was first shown by resolving the photosystem I-II supercomplex of red algae *in situ* at an overall resolution of 3.2 Å [7]. A similar approach was later applied to determine structure of the respiratory chain supercomplexes at 2.8 Å resolution (locally up to 1.8 Å) in unthinned mitochondria isolated from procine tissue [9]. To robustly identify particles in the crowded cellular environment using 2D projections of small cellular volumes for *in situ* SPA, several two-dimensional template matching (2DTM) algorithms have been developed [10-13]. Those programs account for the background noise of overlapping densities from other molecules by applying either whitening filters [10,13] or a frequency-dependent signal-to-noise scoring function [11]. 2DTM not only provides the x- and y-coordinates of the target molecule in the micrograph but also estimates the Euler angles and the z-position by searching across different contrast transfer function (CTF) values. Three software packages have been developed for this purpose and are available as free tools, including GiSPA [14], cisTEM [13], and HRTM [10].

The advantage of *in situ* single-particle EM compared to tomography is the significantly higher throughput, with acquisition times in the order of seconds compared to minutes when tomographic tilt series collections [15]. However, the downside is that the entire content of the respective lamella is projected into 2D. Unlike tomography, there is no opportunity to computationally remove structural noise from regions above and below the target molecule to enhance the contrast of the specific tomographic z-slice. Hence, although *in situ* single-particle cryo-EM remains a viable alternative to tomography, the significantly higher

background noise from cellular components in 2D imaging limits contrast and SNR, consequently, the ability to resolve molecules at high resolution, generally restricting analysis to large molecular assemblies[14].

For *in situ* data collections, the sample must be thin enough to allow sufficient penetration of the electron beam through the tissue or cellular sample, while at the same time minimizing the damage to the biological material caused by inelastic scattering [16]. In practice, the sample thickness for *in situ* studies is usually kept around the inelastic mean free path of the electrons, which depends on the accelerating voltage (e.g., 200 nm at 120 kV and ~350 nm at 300 kV) [17,18]. Typically, samples between 100 and 200 nm in thickness are prepared and should not exceed 500 nm. Several strategies were applied to achieve this: (i) Using cells or viruses that are thin enough to image directly (e.g., *Mycobacteria* with widths of 0.2–0.5 µm) [19,20], (ii) Imaging the cell cortex or the leading edge (lamellipodia of mouse embryonic fibroblasts) [10], which is typically thin enough to be penetrated by the beam (0.1–0.5 µm) , (iii) Focused ion beam (FIB) milling to thin the sample to a desired thickness (0.1–0.5 µm) to generate a thin lamella suitable for data collection [21-23]. The latter became the most widespread technique, as it is not limited to specific cell or tissue types. However, FIB milling of biological specimens also has several major drawbacks. First, the volume of specimens located above and below the chosen imaging section within the cells will be irreversibly removed and cannot be used for additional data collection of potentially interesting areas in those parts of the cell **(Fig. 1a)**. In addition, the radiation damage caused by the ion or plasma beam during removal of the biological material is substantial and can penetrate as deep as 30–60 nm from the surface of the lamella [16,24]. This means that, for instance, in a 100 nm thick lamella, optimally only about 40 nm of the biological material at the center remains undamaged, whereas in the worst-case scenario, the entire volume of the lamella exhibits significant radiation damage. Furthermore, the detection of fluorescence-labeled proteins using Cryogenic Correlative Light and Electron Microscopy (Cryo-CLEM) in the z-direction remains challenging for FIB-milled lamellae, as identification of the z-plane in which the target resides is not very accurate **(Fig. 1a)** [25,26]. Additionally, although recent technical advancements using plasma-based FIB scanning electron microscopes (FIB-SEM) which improved milling speeds substantially [27], FIB milling remains a relatively low throughput method [1]. Automated FIB lamella generation typically produces only about 20 lamellae per day, which is also limited by the buildup of ice contamination from residual water molecules in the vacuum column on the freshly prepared lamellae over time [28]. Finally, the thickness of FIB-generated lamellae has a lower limit of about 100 nm [16,24]. Going thinner than this leads to ion beam-induced damage within the lamella, leaving basically no undamaged region that could be imaged. However, to determine high resolution structures of smaller proteins, thinner lamellae are required to achieve sufficiently good contrast and SNR [6,14].

An alternative approach for producing thin sample of vitrified biological material is the use of cryo-electron microscopy on vitreous sections (CEMOVIS)[29-32]. The technique uses high-pressure freezing (HPF) to cryofix a sample [33-35], typically 100-200 µm thick, followed by slicing it into ultrathin sections using diamond knives [36]. This overcomes most of the previously described limitations found for FIB-milled samples. CEMOVIS can produce sections as thin as 25–30 nm, which is within the same thickness range as the ice layers used in plunge-frozen samples for SPA [37]. Surface damage caused by knife marks depends on the knife radius of curvature and is believed to be limited to 5 nm on each side of the section [38]. Importantly, the method is considered non-destructive in the z-direction, as all sections remain physically connected and are laid out sequentially like a film strip (ribbon) onto the EM grid **(Fig. 1a)**. This is especially useful for determining the positions of fluorescence-labeled proteins in cryo-CLEM-based targeted detection, without loss of adjacent sections in the z-direction **(Fig. 1a)** [39]. CEMOVIS is also a high-throughput method, capable of generating several hundreds, of sections within a few hours (cryo trimming and sectioning) without significant ice contamination buildup. However, cutting high-quality sections is not trivial and requires highly skilled personnel [29]. Additionally, even the best sections will inevitably suffer from knife marks on the surface and, more critically, from compression artifacts in the cutting direction (up to 60%) [40]. This compression becomes increasingly severe as the section thickness decreases and may dampen all high-resolution signals of any macromolecules present in the cellular ultrastructure [40,41]. Most studies using CEMOVIS have been carried out at low resolution [39,42,43] and it is well known that compression deforms the cellular environment at low magnification scale. Though, it remains unclear whether compression also affects the macromolecular scale, and if high-resolution structure determination (<4 Å) using vitreous sections is feasible. Here, we report a 2.98Å *in situ* structure of the bacterial 50S ribosomal large subunit, demonstrating for the first time that sub-3 Å structural determination is possible using high-quality vitreous sections from *E. coli* cells. In addition, we show that this technique can also be applied to purified macromolecules, offering a potential solution to the preferred orientation problem frequently encountered in single-particle plunge-frozen samples. Finally, we discuss potential sources of compression artifacts and propose future directions aimed at eliminating or minimizing these, with the goal of establishing CEMOVIS as a viable alternative for *in situ* cryo-EM studies.

**Results:**

**Cutting ultrathhin vitreous sections from *E. coli* cells optimized for SPA.**

The schematic in **Extended Data Fig. 1** summarizes the various types of damage that can occur during the cutting of vitrified biological material using CEMOVIS. However, if performed under optimal conditions,

all cutting artefacts can be eliminated or minimized, except for surface knife marks and compression caused by the cutting force. For example, crevasses can be avoided by cutting sections thinner than 50 nm. In HPF for CEMOVIS, dextran (20-40% w/v) is commonly added as a cryoprotectant to achieve sample vitrification [31]. Dextran also facilitates smoother sectioning due to its plastic-like properties after vitrification. Since we aimed for SPA, we used a very dense suspension of *E. coli* cells to ensure their presence in as many acquisition areas as possible (**Extended Data Fig. 2a)**. This allowed us to reduce the dextran concentration to 10%, as the high cell density displaced water between the cells, thereby reducing the need for cryoprotectant. Following vitrification of the *E. coli* suspension, the sample was sectioned using a cryo-ultramicrotome. Sections were cut as thin as possible, with nominal thicknesses (feed) ranging from 30 to 50 nm. They were attached to conventional copper EM grids (Quantifoil 1.2/1.3, Cu 300) by electrostatic charging **(Fig. 1b)** [44]. We observed that the smaller 1.2 µm holes stabilized the sections more effectively than the larger 2 µm holes, likely due to their narrower geometrical constraints and hence better mechanical support. Additionally, we found it crucial to attach the sections to a grid surface free of contamination. Any residual ice present on the grid prior to section attachment led to poor adhesion and high drift during data collection. No additional modifications, such as carbon or other types of coatings, were required to stably attach the sections to the grids. The process yielded approximately 130 sections per 30 minutes, demonstrating the high-throughput capabilities of the method **(Supplementary Video 1)**. Inspection of the vitreous sections at various magnification levels showed high quality, crevasse-free, densely packed *E. coli* cells, suitable for data collection using SPA **(Fig. 1c–e)**.

**SPA of purified 50S large ribosomal subunit (LSU) at 2.75 Å resolution from vitreous sections without orientation bias.**

The obtained high-quality sections from cells prompted us to investigate whether high-resolution structure determination could be achieved, first in a simplified *in vitro* system. Our reasoning was that if purified ribosomes were high-pressure frozen and sliced into ultrathin sections for imaging, their orientations in the microscope should be entirely random **(Fig. 2a)**. This is in contrast to plunge freezing, where the air-water interface and thin ice layer often lead to preferred orientations [45].

We prepared highly concentrated bacterial ribosomes to aim HPF followed by sectioning (**Extended Data Fig. 2b)**. Previous reports indicated that single-particle structures can, in principle, be determined in the presence of cryoprotectants [46]. However, we removed dextran entirely to achieve the best possible contrast and SNR. We reasoned that the high concentration of isolated ribosomes would itself act as an effective cryoprotectant and enable full vitrification upon HPF. Ribosomes were cryofixed without the use of

cryoprotectant using HPF, however, we employed a customized 25 µm carrier (Wohlwend GmbH, Sennwald, Switzerland) to minimize the sample volume and ensure full vitrification. There were no signs indicating significant crystalline ice formation, demonstrating that the sample was fully vitrified **(Fig. 2b)**. Motion correction and CTF estimation were performed using cryoSPARC [47] and revealed usable signal up to a resolution of 3.3 Å **(Fig. 2b)**. The data was processed in cryoSPARC **(Extended Data Fig. 3)**. We used template particle picking followed by particle extraction and 2D classification. However, the initially obtained 2D class averages were blurry, presumably due to the presence of too many viewing angles and too few particles per angle. To overcome this, a 50S ribosome map reconstructed from the same sample under conventional plunge-freezing conditions (in buffer) was used as a 3D reference in heterogeneous refinement, together with four junk classes **(Extended Data Fig. 4)**. Several iterative rounds of 3D classification and refinement using this reference allowed to enrich for ribosomal particles. Using those resulted in a final reconstruction of the 50S ribosomal subunit at 2.75 Å resolution **(Extended Data Fig. 5)**. As a control, 2D classification using those curated set of high-quality particles was performed. The classes remained blurry but when we increased the number of iterations to 300, clear 2D class averages from a wide range of views were obtained **(Fig. 2b)**. Comparison of the angular distribution with a plunge-frozen reference dataset showed that orientation bias was completely absent, and all views were equally represented **(Fig. 2c)**. Comparison of the 50S subunit map from plunge-frozen samples with the *in vitro* reconstruction from vitreous sections shows no significant damage or differences, suggesting that compression does not significantly affect the macromolecular structure **(Extended Data Fig. 6)**.

In conclusion, we demonstrate that structure determination at 2.75 Å resolution is possible using purified proteins from vitreous sections, and that this approach can overcome the orientation bias problem. Moreover, our results suggest that starting the analysis in 3D is advantageous, as all orientations are present, making particle enrichment more efficient in 3D than in 2D classification.

**Damaged 70S ribosomes (monosomes) particles arise due to size limitation of ultrathin sections.**

In the dataset, we were also able to detect monosomes. However, we observed that the 30S subunit and the central protuberance (CP) region of the monosome appeared fuzzier than expected, suggesting that some form of damage may have occurred. Size measurements of the low-pass filtered map from the plunge-frozen monosome indicated that the intact part of a vitreous section must be at least 28 nm thick to accommodate the full ribosome, including more flexible regions such as the L7/L12 stalk **(Fig. 3a)**. To estimate the thickness of our sections, we collected 18 tilt series from *in situ*-generated vitreous sections, reconstructed tomograms for each of them, and measured the section thickness at multiple sampling points

**(Fig. 3b)**. A mean section thickness of 48.36 ± 3.74nm was estimated **(Fig. 3c)**. This value reflects the actual section thickness after compression has occurred. However, the critical parameter that determines whether an object was damaged during the cutting process due to the object size is not this compressed thickness $t'$, but the nominal feed value, denoted as $f$, set at the microtome i.e. before compression has occured. The relationship between the feed thickness $f$ and the actual section thickness $t'$ is given by the equation (2) **(Extended Data Fig. 1)**. Hence, the feed thickness $f$ is estimated to be approximately 40 nm. Additionally, knife marks typically reduce the usable thickness by about 5 nm from each side, leaving only a ~30 nm undamaged central zone in the section **(Fig. 3d)**. This model allows us to calculate the probability that a spherical object will end up within this undamaged zone. The expected probability can be estimated using Equation (3) and is only 15% for the 50S subunit and 5% for the monosome **(Fig. 3d–e)**. Further theoretical considerations show that even if the section thickness is increased to 50 nm, the point at which crevasses begin to form, the probability of a large object, such as the 70S ribosome, ending up undamaged in the central region still remains low (25%) **(Fig. 3e)**. Thus, cutting thicker than 50 nm would introduce surface damage in form of crevasses, which would in turn damage particles located beneath these cracks. Therefore, CEMOVIS is best suited for smaller molecular targets (e.g., <50S subunit). First, because larger proteins may be physically damaged during sectioning, and second, because the relatively thin vitreous sections, as compared to thicker FIB-milled lamellae, provide better contrast and SNR required for *in situ* SPA of small macromolecules .

### *In situ* 2.98 Å reconstruction of the ribosomal LSU using SPA and vitreous sections from bacterial cells.

We next used the vitreous sections prepared in **Fig. 1** and collected data for SPA. The motion correction and CTF estimation for the in situ data showed fitting comparable to the in vitro dataset **(Fig. 4a)**. Again, we started with 3D heterogeneous refinement using the map obtained from the plunge-frozen dataset as a reference. To separate the undamaged from the damaged particles, several classification steps were required. However, the limited number of particles restricted the number of classification rounds, and only a small subset of particles remained after several iterations. To increase the number of particles identified from the micrographs, we applied GisSPA 2DTM [14] on the motion-corrected micrographs using the LSU from the plunge-frozen reference as the search model. We were able to match 122k ribosomes **(Fig. 4b–c)**, from which, after several rounds of classification, a reconstruction at 2.98 Å resolution was obtained using 40,187 particles in RELION [48] **(Extended Data Fig. 7)**. The map shows high-resolution features at the

side-chain level **(Fig. 4d)**. The CP region and some rRNA segments on the surface of the ribosome show more flexibility than usual **(Fig. 4d)**, presumably due to the *in situ* context, where increased flexibility is expected. To show that the CP region, although more flexible, is still intact, we performed focused refinement using a smaller mask centered on the CP region **(Fig. 4d)**. The analysis shows that the density exhibits the typical expected improvement, indicating that the internal integrity of the CP is preserved. In summary, we obtained a high-resolution reconstruction of the *E. coli* 50S ribosome *in situ* using vitreous sections and SPA, showing for the first time that CEMOVIS is a valid alternative method to study macromolecules *in situ* at <3 Å resolution.

**Discussion:**

In this work, we demonstrate for the first time using single-particle cryo-EM that high-resolution structure determination from vitreous sections at sub-3 Å resolution is possible for both isolated and *in situ* 50S ribosomes. Two recent studies similarly demonstrate the potential of CEMOVIS for high-resolution structural studies. The first study used CEMOVIS to produce 150–200 nm thick sections of high-pressure frozen lysozyme nano crystals as a novel approach in electron diffraction experiments [49]. The authors concluded that the main advantage of the method is its high throughput of protein structural determination by electron diffraction, enabled by the large number of crystals that can be produced using CEMOVIS and the reduced background noise resulting from the removal of surrounding solvent through the sectioning process. The more recent study showed that *in situ* determination of the 60S ribosomal subunit in yeast cells is feasible using SPA applied to 100 nm-thick sections prepared by CEMOVIS. However, the resolution was limited to above 3 Å, likely due to the poor quality of the sections, which exhibited severe cutting artifacts caused by crevasses. Crevasses are cracks in the surface that extend deep into the section that increase with section thickness, creating dark areas unsuitable for data collection and damaging the underlying biological material. Unlike our present work, the authors reported problems with the attachment of their sections to the grids. These attachment difficulties can be explained by the greater thickness, which typically leads to significantly increased surface deformations and, consequently, poor section attachment. Moreover, thicker sections possess greater mass, which in our experience significantly compromises their stable attachment. This is likely due to the insufficient effect of electrostatic charging to adhere the vitreous sections to the support film of the EM grid. Hence, coating or other grid modifications are not needed for stable attachment but requires high-quality sections with a thickness below 60 nm to be suitable for data collection with minimal drift as well as better contrast and SNR.

We optimized CEMOVIS for smaller macromolecules by producing sections as thin as 30 nm, which improves the SNR and enables high-resolution structure determination. When sections are cut under optimal conditions, most artifacts can be minimized or completely avoided, except for compression and knife marks in the cutting direction. The knife marks in CEMOVIS are only 3–5 nm in extent, which is significantly less than the surface damage typically seen in FIB-milled lamellae (30–60 nm) [16,24]. While compression remains a concern for large-scale deformations of the cellular environment, structural integrity at the macromolecular level appears to be preserved. This is supported by our successful reconstruction of intact 50S ribosomal particles in sections of isolated ribosomes and *in situ*. Nevertheless, further efforts are needed to enable a compression-free sectioning process that fully preserves the cellular environment, to establish CEMOVIS as a robust accepted method not only for high-resolution structure determination but also for analysis of the overall cellular architecture. We propose two promising directions to address the compression problem. First, as described by Equation (1) in **Extented Data Fig. 1**, compression decreases with the cutting angle α. A decrease in compression with decreasing knife angle was also shown experimentally [50,51]. This implies that at a knife angle of 0°, no compression would occur. Currently, however, knives are too fragile to use at angles lower than 25°. Future development to improve knifes may help overcome this limitation. Second, we showed that compression-free vitreous sections can be produced using an oscillating knife which virtually reduces the cutting angle down to 0° [38,41]. Although the reproducibility was insufficient, the method was not extensively optimized, and technical advancements in oscillating knife technology over the last two decades may have improved the precision of the process. These technical developments will not only enable the production of compression-free vitreous sections but also eliminate crevasses in thicker sections, thereby extending the applicability of CEMOVIS to large macromolecular complexes.

The major advantage of CEMOVIS lies in its ability to produce much thinner sections with minimal surface damage and significantly higher throughput compared to FIB-milled lamellae. Such thin sections with minimal surface damage are not achievable with current FIB-milling techniques, as FIB introduces damage up to 60 nm from each side, limiting lamella thickness to 100–150 nm. Nevertheless, we observed in our study that monosomes suffer from degradation, as indicated by the fuzzy densities of more flexible elements such as the CP and the 30S small subunit. Several scenarios could explain the source of this damage. One possibility is that HPF might compromise the molecular integrity. However, a recent study demonstrated that intact monosomes can be obtained from high-pressure frozen samples, ruling out this explanation [52]. That study achieved a ribosome reconstruction at ~4 Å resolution, confirming structural preservation. Another possibility is that compression during sectioning causes damage at the macromolecular level. In our study, the 50S large subunit remained intact, making it unlikely that compression accounts for the

observed damage to the monosome. Importantly, monosomes show damage specifically in fragile regions, such as CP region of the 50S subunit, which are generally flexible and likely the first regions to be affected. Yet, the same region appear preserved in isolated 50S subunits, further indicating that compression is not the primary cause of monosome degradation. We therefore conclude that the monosome is simply too large to fit within the undamaged zone of 30 nm-thick sections. Our analysis, shown in **Fig. 3**, supports this idea. Nervertheless, we cannot rule out that some damage might have occurred, and we were unable to separate the damaged from the undamaged particles by classification, as classification is not perfect. Collecting larger datasets might increase the number of undamaged particles, thereby allowing more reliable separation from the damaged ones. To obtain high-resolution monosome reconstructions, thicker sections would be required to statistically accommodate entire monosomes within the undamaged interior of the sections. However, there is a size limit, as sections thicker than 50 nm typically develop crevasses, leading to additional sources of damage. Thus, while the method is ideally suited for smaller macromolecules, it is currently more challenging to apply to larger complexes. Finally, the method appears to be limited by the section thickness when applied to smaller molecules, and future work should clarify whether high-resolution reconstructions can also be obtained for molecules with a molecular weight below 0.5 MDa.

In conclusion, we demonstrate that CEMOVIS is a valid technique for high-resolution structure determination at the macromolecular scale, both *in situ* and *in vitro*. Future efforts will focus on overcoming compression artifacts to establish CEMOVIS as a widely adopted method for *in situ* structural biology both at the ultrastructural and macromolecular levels.

**Methods:**

***E. coli* culture and preparation of a highly concentrated cell suspension suitable for HPF.**

*E. coli* cells (BL21) were plated onto conventional LB agar plates and grown overnight at 37 °C. The next day, a single colony was picked and inoculated into a 50 ml Falcon tube containing 20 ml of LB medium. This starter culture was grown overnight at 37 °C and 220 rpm in a shaking incubator. On the following day, three 1-liter flasks, each containing 200 ml of LB medium, were inoculated with 1 ml, 5 ml, and 10 ml of the overnight culture, respectively, and incubated at 37 °C and 220 rpm. $OD_{600}$ was monitored continuously at 30-minute intervals. Once one culture reached an $OD_{600}$ of 0.4, it was harvested by centrifugation for 10 minutes at 4,000 × g using an F14-6x250y rotor at 4 °C. The resulting pellet was resuspended in 10 ml of 1× PBS and centrifuged again at 4,000 × g for 10 minutes at 4 °C using a SX4250 rotor. The final pellet (5 ml) was carefully resuspended in 5 ml of 20% dextran (prepared in 1× PBS). From this suspension, 1 ml was transferred into a 1.5 ml Eppendorf tube and centrifuged for 10 minutes at 4 °C

at 4,000 × g. The supernatant was removed, and the resulting paste-like pellet was directly used for high-pressure freezing.

**Purification of ribosomes from *Escherichia Coli* (*E. coli)* cells.**

To purify ribosomes from *E. coli* cells, we followed the protocol described by Yi Cui *et al.,* 2022 [53]. In brief, the LB culture described in the previous section was grown to an $OD_{600}$ of ~0.9. The culture was harvested by centrifugation at 4,000 × g for 10 minutes at 4 °C. The resulting 2.7 g pellet was carefully resuspended by pipetting up and down in a 50 ml Falcon tube using 12 ml of Buffer A (50 mM Tris-acetate, pH 7.7; 60 mM potassium glutamate; 14 mM magnesium acetate). Then, 700 µl of 5 mg/ml lysozyme (prepared in Buffer A) were added, and the suspension was incubated for 30 minutes at 37 °C with shaking at 700 rpm. The cell suspension was then subjected to freeze-thaw cycles in liquid nitrogen to lyse the cells and release the lysate. Subsequently, 20 µl of DNase I (Invitrogen, 18047-019) were added to degrade genomic DNA, and the mixture was incubated for 1 hour at 4 °C. The lysate was cleared by centrifugation at 10,000 rpm for 1 hour at 4 °C using a F14-6x250y rotor. The resulting supernatant (~20 ml) was filtered through a 0.22 µm filter to remove residual debris. The filtrate was then diluted with 20 ml of Buffer B (20 mM Tris-HCl, pH 7.7; 500 mM ammonium chloride; 10 mM magnesium acetate; 0.5 mM EDTA; 30% sucrose; 7 mM β-mercaptoethanol). This mixture was centrifuged at 170,000 × g (average) for 1.5 hours at 4 °C. The supernatant was discarded, and the pelleted ribosomes were washed with 500 µl of Buffer C (20 mM Tris-HCl, pH 7.7; 6 mM magnesium acetate; 30 mM potassium chloride; 7 mM β-mercaptoethanol). Finally, the pellet was resuspended in 50 µl of Buffer C.

**Grid preparation and data acquisition of plunge-frozen *E. coli* ribosomes.**

For the reference dataset, we used the same purified sample as for the isolated ribosomes in vitreous sections. Quantifoil R2/2 copper grids with a 2 nm carbon support layer and 300 mesh size (100 pieces, Jena Bioscience) were glow-discharged using a GloQube Plus instrument (Quorum Technologies, UK) for 30 seconds at 35 mA. The purified bacterial ribosomes were centrifuged at maximum speed for 10 minutes at 4 °C to pellet aggregated proteins. From the resulting supernatant, 3 µl was applied onto the Quantifoil grids and incubated for 30 sec in the 100% humidity chamber of a Vitrobot Mark IV (FEI Company, USA). The grid was blotted for 3 sec and subsequently plunge-frozen in liquid ethane. Grids were clipped and loaded into a 300-kV Titan Krios G4 microscope (Thermo Fisher Scientific, EPU v3.5.1.6034 software) equipped with a Selectris Energy filter (Slit width 10 eV) and a Falcon 4i direct electron detector (Thermo Fisher Scientific). Grids were screened for quality control based on particle distribution and density, and

images from the best grids were recorded. Micrographs were recorded at a nominal magnification of 165,000x, corresponding to a calibrated pixel size of 0.729 Å. The dose rate was 8 electron per physical pixels per second, and images were recorded for 3 s in the EER format, corresponding to a total dose of 40 electrons per Å2. Defocus range was set between −0.5 µm and −2 µm. Gain-corrected image data were acquired.

**Cryo-EM data processing of plunge-frozen *E. coli* ribosomes**

Processing was started in cryoSPARC Live v4.6.0 [47] with motion correction, CTF estimation, and blob picking. A total of 385,834 particles were picked and extracted using a 192-pixel box size (Fourier-cropped from 500 pixels) and used for 2D classification. The high quality 2D class averages were subjected to *ab initio* job with 4 classes as input. The best class was refined to 3.9 Å, and this map was then used as input for heterogeneous refinement with two good classes and three junk classes, using all 385,834 picked particles as input. The best class contained 124,933 particles and was refined to a resolution of 3.01 Å. This particle set was also exported to RELION [48] and re-extracted without binning using a 500-pixel box. After refinement followed by classification into 4 classes, the class corresponding to the 50S ribosomal subunit was used for a final refinement, which resulted in a map at 3.16 Å resolution.

**High-Pressure Freezing (HPF)**

Two types of samples were prepared for high-pressure freezing: purified *E. coli* ribosomes and dense *E. coli* cell pellets. Purified ribosome suspensions were loaded into custom-fabricated 25 µm-deep membrane carriers (Wohlwend GmbH, Sennwald, Switzerland) without any cryoprotectant. The ribosome was concentrated to 34 ug/ul which was sufficient to ensure efficient heat transfer and achieve vitrification upon rapid freezing. Dense *E. coli* cell pellets were prepared as described above. These cell pellets were then loaded into standard 100 µm-deep membrane carriers (Leica Microsystems).

All samples were vitrified using an EMPACT II high-pressure freezer (Leica Microsystems) at ~2100 bar and cooling rates exceeding 20,000 °C/s. Immediately after freezing, carriers were transferred into pre-cooled metal storage boxes under liquid nitrogen to maintain vitrified conditions. Sample carriers were stored in liquid nitrogen until further processing. HPF conditions, including pressurization rates and cooling curves, were monitored using the EMPACT II's onboard diagnostic tools to ensure reproducibility across preparations.

**Cryo-Ultramicrotomy and CEMOVIS**

Frozen carriers were mounted under liquid nitrogen into a Leica EM UC7/FC7 cryo-ultramicrotome (Leica Microsystems). Prior to sectioning, sample faces were trimmed using a cryo-trimming knife to expose the vitrified material and to produce a sample block with a side ~ 100 µm for cryosectioning. Ultrathin vitreous sections with a feed ranging from 30–50 nm were cut at –140 °C using a 35° CEMOVIS or cryo-immuno diamond knife (Diatome Ltd., Nidau, Switzerland), with a cutting speed of 0.5–1.0 mm/s.

Sections were collected onto 300 mesh copper Quantifoil R1.2/1.3 grids (Quantifoil Micro Tools GmbH) using a double micromanipulator system, ensuring minimal contact and mechanical stress. Section gliding on the knife surface was made smooth by using the electrostatic discharging with the ionizer. Attachment of the vitreous sections on the EM grids were performed by electrostatic charging for a few seconds. Each grid was visually inspected under the microtome stereomicroscope to assess section quality, integrity and good attachment. Grids were stored in a firmly closed cryo-grid boxes inside the cryo-ultramicrotome and maintained at cryogenic temperatures throughout transport to the cryo-electron microscope for subsequent cryo-electron tomography or single-particle cryo-electron microscopy.

**Data collection and SPA processing of purified ribosomes from vitreous sections**.

The state of vitreous water was verified using the electron diffraction.

Data were collected on a Titan Krios G4 microscope (Thermo Fisher Scientific) equipped with a Falcon 4i camera and a Selectris energy filter (slit width: 10 eV) from vitreous sections of purified ribosomes using EPU software (v3.5.1.6034) at a magnification of 165,000×, corresponding to a pixel size of 0.73 Å/pixel. A total of 8,435 movies were acquired with a total dose of 40 $e^{-}/Å^{2}$ and a defocus range of –0.7 µm to –2.5 µm.

**Extended Data Fig. 3** illustrates the data processing workflow for isolated *E. coli* ribosomes prepared by HPF and CEMOVIS. The following pre-processing steps were performed with cryoSPARC Live v4.6.0 [47]. Movie stacks were motion-corrected and dose-weighted using MotionCor2 v2.1.1 [54]. Contrast transfer function (CTF) estimates for the motion-corrected micrographs were calculated with CTFFIND4 v4.1.13 [55]. Particles were autopicked using 44 of the representative 2D classes averages containing different orientations as templates prepared from the plunge-freezing data. This resulted in 946,839 picked particles from 8,435 micrographs. Each particle was extracted at a box size of 96 pixels (5.2x binned). Subsequent image processing was carried out with cryoSPARC v4.6.0. An initial model generated from the plunge-freezing data was used as a reference volume to clean up the particles. Particles were classified by three

rounds of three-dimensional (3D) heterogeneous refinement using 5 classes. Particles were then re-extracted at 500 pixels (unbinned) and an initial model was generated. Analysis of the initial model identified only LSU in the reconstruction. The initial model was subsequently used for homogeneous refinement followed by non-uniform (NU) refinement to get a reconstruction at 3.7 Å overall resolution with C1 symmetry. CTF refinement (without 4th order aberrations) followed by another round of NU refinement improved the quality of the reconstruction. Particles were converted into a STAR file and input into RELION v5.0 for further processing [48].

Particles were re-extracted at 500 pixels (unbinned) followed by 3D refinement using the cryoSPARC map as the starting model. CTF refinement (without 4th order aberrations) followed by another round of 3D refinement improved the quality of the reconstruction. 'Polished' particle images, which were corrected for individual particle movements, were generated using aligned movie frames that were output from MotionCor2. Subsequent 3D refinement on the polished particles, resulted in reconstruction at 3 Å overall resolution with C1 symmetry. Further CTF refinement (without 4th order aberrations), Bayesian Polishing and 3D refinement improved the quality of the reconstruction to 2.74 Å overall resolution with C1 symmetry. To remove the particles that have been damaged by the CEMOVIS preparation, 3D classification was performed (without alignment) on the particles using five classes and a T value of 4. A class with 45% distribution and 51,328 particles was identified. Subsequently, the particles from this class were subjected to 3D refinement, CTF refinement, 3D refinement, Bayesian polishing and 3D refinement to yield a reconstruction to 2.74 Å overall resolution with C1 symmetry. Analysis of the angular distribution of the refined particles showed no orientation bias in comparison to the particles from the plunge-freezing data, which suffer major orientation bias **(Fig. 2c)**.

In order to improve the density for the CP region of the LSU, focused 3D classification (without alignment) was performed on the consensus map using three classes and a T value of 4 with a mask covering the CP region of the LSU. Local 3D refinement of a class containing 34,616 particles using the same mask covering the CP region improved the density in this region.

All final reconstructions were sharpened using RELION post-processing. The local resolution estimations in **Extended Data Fig. 5** were performed using RELION.

### ***In situ*** **data acquisition and SPA processing of 50S ribosomes from vitreous sections.**

Grids containing vitreous sections from bacterial cells were imaged using a total electron dose of 40 $e^{-}/Å^{2}$. A magnification of 165,000× was used on a Titan Krios G4 microscope (Thermo Fisher Scientific)

equipped with a Falcon 4i camera and a Selectris energy filter (slit width: 10 eV), corresponding to a calibrated pixel size of 0.729 Å. In EPU software (v3.5.1.6034), automated hole detection algorithms did not perform reliably, so most holes were selected manually. The defocus range was set between –0.7 µm and –2.5 µm. A total of 28,790 movies were recorded and subsequently gain-corrected. Movies were initially imported into cryoSPARC Live v4.6.0 for motion correction [47]. Blob picking was used to identify particles across the micrographs, and 3D heterogeneous refinement was performed using the plunge-frozen 50S ribosome reconstruction as the reference. However, after several rounds of classification and refinement, it became evident that too few particles remained to obtain an intact 50S ribosomal subunit at side-chain-level resolution. Therefore, we adopted a different processing strategy, as outlined in **Extended Data Fig. 7.** The movies were imported into RELION 5.0 [48], and motion correction was repeated using MotionCor2 [54]. Particle identification was carried out using GisSPA 2DTM software [14] with the plunge-frozen 50S map as the search model and a score threshold of 6.8. This resulted in the detection of 145,133 particles, which were extracted in a 500-pixel box without binning. A 3D classification without alignment or mask was performed using 3 classes, a T-value of 4, and an E-value of –1. The best class (86%) contained approximately 120,000 particles, which were then subjected to alternating rounds of CTF refinement and Bayesian polishing, resulting in a consensus reconstruction at 2.96 Å resolution. In a second processing branch, several classification steps were performed to remove damaged particles. The first classification focused on the CP region using a mask covering the entire CP (T = 10, E = 4). The best class (60.5%) was selected for further processing. A subsequent classification used a peripheral mask (2 classes, T = 10, E = 4), and the best class (81.5%) was used in a final classification round covering the entire 50S subunit (2 classes, T = 10, E = 4). The best class (80.6%) was selected from the polished dataset and refined, resulting in a 2.98 Å consensus map. Finally, a focused refinement was carried out using a smaller mask on the CP region to improve local resolution.

**Model building and refinement.**

The 50S LSU structure published in the PDB under the accession number 6PJ6 was rigid-body fitted using Chimera [56] into the *in vitro* and *in situ* maps of the structures determined from vitreous sections. This was followed by flexible fitting using Coot v0.9.8.95 [57] with activated self-restraints. The model was then manually refined in real space using Coot to correct side-chain torsions and other local deviations from the original model. The models were subsequently imported into ISOLDE [58] to correct all rotamer outliers, Ramachandran outliers, and to improve clash scores. Final refinement was performed using real-space refinement in PHENIX [59], and validation was carried out using the PDB validation server. Iterative

refinement with manual model building in Coot was continued until the model quality and model-to-map fit were sufficiently high. All figures were prepared using Chimera X [60].

**Data availability**

The atomic coordinates of the bacterial ribosome structures obtained from vitreous sections were deposited in the Protein Data Bank under accession codes XXXX (*in situ*) and XXXX (*in vitro*). The corresponding density maps were deposited in the EMDB under accession codes EMD-XXXX and EMD-XXXX, respectively. The map from the plunge-frozen reference dataset was deposited in the EMDB under the accession code EMD-XXXX.

**Acknowledgments**

This work was financed via the KAUST Baseline Fund. We thank the members of the IAC-EM Core Lab at KAUST, Lingyun Zhao, Alessandro Genovese and Rachid Sougrat for their continuous support with cryo-EM data collection and for maintaining the microscopes and associated equipment.

**Author Contributions Statement:**

AN and AA designed this study. AA prepared all vitreous sections used in this study. RB purified the ribosome sample and collected the *in vitro* data from vitreous sections. XY and RB prepared the cell suspensions for the *in situ* studies. AN, AA and RB collected and processed the *in situ* data. AN built the atomic model. All authors jointly analyzed the data, prepared the figures, and wrote the manuscript.

**Competing Interests Statement**

The authors declare no competing interests.

**References**

1 Noble, A. J. & de Marco, A. Cryo-focused ion beam for in situ structural biology: State of the art, challenges, and perspectives. *Current Opinion in Structural Biology* **87**, 102864 (2024). https://doi.org:https://doi.org/10.1016/j.sbi.2024.102864

2 Young, L. N. & Villa, E. Bringing Structure to Cell Biology with Cryo-Electron Tomography. *Annu Rev Biophys* **52**, 573-595 (2023). https://doi.org:10.1146/annurev-biophys-111622-091327

3 Tegunov, D., Xue, L., Dienemann, C., Cramer, P. & Mahamid, J. Multi-particle cryo-EM refinement with M visualizes ribosome-antibiotic complex at 3.5 A in cells. *Nat Methods* **18**, 186-193 (2021). https://doi.org:10.1038/s41592-020-01054-7
4 Xing, H. *et al.* Translation dynamics in human cells visualized at high resolution reveal cancer drug action. *Science* **381**, 70-75 (2023). https://doi.org:10.1126/science.adh1411
5 Zheng, W. *et al.* Visualizing the translation landscape in human cells at high resolution. *bioRxiv* (2024). https://doi.org:10.1101/2024.07.02.601723
6 Rickgauer, J., Choi, H., Lippincott-Schwartz, J. & Denk, W. *Label-free single-instance protein detection in vitrified cells*. (2020).
7 You, X. *et al.* In situ structure of the red algal phycobilisome-PSII-PSI-LHC megacomplex. *Nature* **616**, 199-206 (2023). https://doi.org:10.1038/s41586-023-05831-0
8 Zhang, X., Xiao, Y., You, X., Sun, S. & Sui, S. F. In situ structural determination of cyanobacterial phycobilisome-PSII supercomplex by STAgSPA strategy. *Nat Commun* **15**, 7201 (2024). https://doi.org:10.1038/s41467-024-51460-0
9 Zheng, W., Chai, P., Zhu, J. & Zhang, K. High-resolution in situ structures of mammalian respiratory supercomplexes. *Nature* **631**, 232-239 (2024). https://doi.org:10.1038/s41586-024-07488-9
10 Rickgauer, J. P., Choi, H., Moore, A. S., Denk, W. & Lippincott-Schwartz, J. Structural dynamics of human ribosomes in situ reconstructed by exhaustive high-resolution template matching. *Mol Cell* **84**, 4912-4928 e4917 (2024). https://doi.org:10.1016/j.molcel.2024.11.003
11 Cheng, J., Li, B., Si, L. & Zhang, X. Determining structures in a native environment using single-particle cryoelectron microscopy images. *Innovation (Camb)* **2**, 100166 (2021). https://doi.org:10.1016/j.xinn.2021.100166
12 Rickgauer, J. P., Grigorieff, N. & Denk, W. Single-protein detection in crowded molecular environments in cryo-EM images. *Elife* **6** (2017). https://doi.org:10.7554/eLife.25648
13 Lucas, B. A. *et al.* Locating macromolecular assemblies in cells by 2D template matching with cisTEM. *Elife* **10** (2021). https://doi.org:10.7554/eLife.68946
14 Cheng, J. *et al.* Determining protein structures in cellular lamella at pseudo-atomic resolution by GisSPA. *Nat Commun* **14**, 1282 (2023). https://doi.org:10.1038/s41467-023-36175-y
15 Eisenstein, F. *et al.* Parallel cryo electron tomography on in situ lamellae. *Nat Methods* **20**, 131-138 (2023). https://doi.org:10.1038/s41592-022-01690-1
16 Tuijtel, M. W. *et al.* Thinner is not always better: Optimizing cryo-lamellae for subtomogram averaging. *Sci Adv* **10**, eadk6285 (2024). https://doi.org:10.1126/sciadv.adk6285
17 Grimm, R., Typke, D., Barmann, M. & Baumeister, W. Determination of the inelastic mean free path in ice by examination of tilted vesicles and automated most probable loss imaging. *Ultramicroscopy* **63**, 169-179 (1996). https://doi.org:10.1016/0304-3991(96)00035-6
18 Diebolder, C. A., Koster, A. J. & Koning, R. I. Pushing the resolution limits in cryo electron tomography of biological structures. *J Microsc* **248**, 1-5 (2012). https://doi.org:10.1111/j.1365-2818.2012.03627.x
19 Xue, L. *et al.* Visualizing translation dynamics at atomic detail inside a bacterial cell. *Nature* **610**, 205-211 (2022). https://doi.org:10.1038/s41586-022-05255-2

20 Turonova, B. *et al.* In situ structural analysis of SARS-CoV-2 spike reveals flexibility mediated by three hinges. *Science* **370**, 203-208 (2020). https://doi.org:10.1126/science.abd5223
21 Young, R. J., Dingle, T., Robinson, K. & Pugh, P. J. A. An application of scanned focused ion beam milling to studies on the internal morphology of small arthropods. *Journal of Microscopy* **172**, 81-88 (1993). https://doi.org:https://doi.org/10.1111/j.1365-2818.1993.tb03396.x
22 Marko, M., Hsieh, C., Schalek, R., Frank, J. & Mannella, C. Focused-ion-beam thinning of frozen-hydrated biological specimens for cryo-electron microscopy. *Nat Methods* **4**, 215-217 (2007). https://doi.org:10.1038/nmeth1014
23 Rigort, A. *et al.* Focused ion beam micromachining of eukaryotic cells for cryoelectron tomography. *Proc Natl Acad Sci U S A* **109**, 4449-4454 (2012). https://doi.org:10.1073/pnas.1201333109
24 Lucas, B. A. & Grigorieff, N. Quantification of gallium cryo-FIB milling damage in biological lamellae. *Proc Natl Acad Sci U S A* **120**, e2301852120 (2023). https://doi.org:10.1073/pnas.2301852120
25 Li, S. *et al.* HOPE-SIM, a cryo-structured illumination fluorescence microscopy system for accurately targeted cryo-electron tomography. *Commun Biol* **6**, 474 (2023). https://doi.org:10.1038/s42003-023-04850-x
26 Pierson, J. A., Yang, J. E. & Wright, E. R. Recent advances in correlative cryo-light and electron microscopy. *Curr Opin Struct Biol* **89**, 102934 (2024). https://doi.org:10.1016/j.sbi.2024.102934
27 Berger, C. *et al.* Plasma FIB milling for the determination of structures in situ. *Nat Commun* **14**, 629 (2023). https://doi.org:10.1038/s41467-023-36372-9
28 Tacke, S. *et al.* A streamlined workflow for automated cryo focused ion beam milling. *J Struct Biol* **213**, 107743 (2021). https://doi.org:10.1016/j.jsb.2021.107743
29 Al-Amoudi, A. *et al.* Cryo-electron microscopy of vitreous sections. *EMBO J* **23**, 3583-3588 (2004). https://doi.org:10.1038/sj.emboj.7600366
30 A, A. L.-A., Dubochet, J. & Studer, D. Amorphous solid water produced by cryosectioning of crystalline ice at 113 K. *J Microsc* **207**, 146-153 (2002). https://doi.org:10.1046/j.1365-2818.2002.01051.x
31 Al-Amoudi, A., Norlen, L. P. & Dubochet, J. Cryo-electron microscopy of vitreous sections of native biological cells and tissues. *J Struct Biol* **148**, 131-135 (2004). https://doi.org:10.1016/j.jsb.2004.03.010
32 Norlen, L., Al-Amoudi, A. & Dubochet, J. A cryotransmission electron microscopy study of skin barrier formation. *J Invest Dermatol* **120**, 555-560 (2003). https://doi.org:10.1046/j.1523-1747.2003.12102.x
33 Han, H. M., Huebinger, J. & Grabenbauer, M. Self-pressurized rapid freezing (SPRF) as a simple fixation method for cryo-electron microscopy of vitreous sections. *J Struct Biol* **178**, 84-87 (2012). https://doi.org:10.1016/j.jsb.2012.04.001
34 Studer, D., Graber, W., Al-Amoudi, A. & Eggli, P. A new approach for cryofixation by high-pressure freezing. *J Microsc* **203**, 285-294 (2001). https://doi.org:10.1046/j.1365-2818.2001.00919.x
35 Moor, H. in *Cryotechniques in Biological Electron Microscopy* (eds Rudolf Alexander Steinbrecht & Karl Zierold) 175-191 (Springer Berlin Heidelberg, 1987).

36 Studer, D., Klein, A., Iacovache, I., Gnaegi, H. & Zuber, B. A new tool based on two micromanipulators facilitates the handling of ultrathin cryosection ribbons. *J Struct Biol* **185**, 125-128 (2014). https://doi.org:10.1016/j.jsb.2013.11.005
37 Henderikx, R. J. M. *et al.* Ice thickness control and measurement in the VitroJet for time-efficient single particle structure determination. *J Struct Biol* **216**, 108139 (2024). https://doi.org:10.1016/j.jsb.2024.108139
38 Al-Amoudi, A., Dubochet, J., Gnaegi, H., Luthi, W. & Studer, D. An oscillating cryo-knife reduces cutting-induced deformation of vitreous ultrathin sections. *J Microsc* **212**, 26-33 (2003). https://doi.org:10.1046/j.1365-2818.2003.01244.x
39 Gilbert, M. A. G. *et al.* CryoET of beta-amyloid and tau within postmortem Alzheimer's disease brain. *Nature* **631**, 913-919 (2024). https://doi.org:10.1038/s41586-024-07680-x
40 Al-Amoudi, A., Studer, D. & Dubochet, J. Cutting artefacts and cutting process in vitreous sections for cryo-electron microscopy. *Journal of Structural Biology* **150**, 109-121 (2005). https://doi.org:https://doi.org/10.1016/j.jsb.2005.01.003
41 Studer, D. & Gnaegi, H. Minimal compression of ultrathin sections with use of an oscillating diamond knife. *J Microsc* **197**, 94-100 (2000). https://doi.org:10.1046/j.1365-2818.2000.00638.x
42 Al-Amoudi, A., Diez, D. C., Betts, M. J. & Frangakis, A. S. The molecular architecture of cadherins in native epidermal desmosomes. *Nature* **450**, 832-837 (2007). https://doi.org:10.1038/nature05994
43 Gunkel, M. *et al.* Higher-order architecture of rhodopsin in intact photoreceptors and its implication for phototransduction kinetics. *Structure* **23**, 628-638 (2015). https://doi.org:10.1016/j.str.2015.01.015
44 Pierson, J. *et al.* Improving the technique of vitreous cryo-sectioning for cryo-electron tomography: electrostatic charging for section attachment and implementation of an anti-contamination glove box. *J Struct Biol* **169**, 219-225 (2010). https://doi.org:10.1016/j.jsb.2009.10.001
45 Kampjut, D., Steiner, J. & Sazanov, L. A. Cryo-EM grid optimization for membrane proteins. *iScience* **24**, 102139 (2021). https://doi.org:10.1016/j.isci.2021.102139
46 Basanta, B., Hirschi, M. M., Grotjahn, D. A. & Lander, G. C. A case for glycerol as an acceptable additive for single-particle cryoEM samples. *Acta Crystallogr D Struct Biol* **78**, 124-135 (2022). https://doi.org:10.1107/S2059798321012110
47 Punjani, A., Rubinstein, J. L., Fleet, D. J. & Brubaker, M. A. cryoSPARC: algorithms for rapid unsupervised cryo-EM structure determination. *Nat Methods* **14**, 290-296 (2017). https://doi.org:10.1038/nmeth.4169
48 Scheres, S. H. RELION: implementation of a Bayesian approach to cryo-EM structure determination. *J Struct Biol* **180**, 519-530 (2012). https://doi.org:10.1016/j.jsb.2012.09.006
49 Moriscot, C., Schoehn, G. & Housset, D. High pressure freezing and cryo-sectioning can be used for protein structure determination by electron diffraction. *Ultramicroscopy* **254**, 113834 (2023). https://doi.org:10.1016/j.ultramic.2023.113834
50 Jesior, J. C. Use of low-angle diamond knives leads to improved ultrastructural preservation of ultrathin sections. *Scanning Microsc Suppl* **3**, 147-152; discussion 152-143 (1989).
51 Richter, K. Cutting artefacts on ultrathin cryosections of biological bulk specimens. *Micron* **25**, 297-308 (1994). https://doi.org:10.1016/0968-4328(94)90001-9

52 Berger, C., Watson, H., Naismith, J., Dumoux, M. & Grange, M. *Xenon plasma focused ion beam lamella fabrication on high-pressure frozen specimens for structural cell biology*. (2024).
53 Cui, Y., Chen, X., Wang, Z. & Lu, Y. Ribosome purification from Escherichia coli by ultracentrifugation. *Biotechnol Notes* **3**, 118-123 (2022). https://doi.org:10.1016/j.biotno.2022.12.003
54 Zheng, S. Q. *et al.* MotionCor2: anisotropic correction of beam-induced motion for improved cryo-electron microscopy. *Nat Methods* **14**, 331-332 (2017). https://doi.org:10.1038/nmeth.4193
55 Rohou, A. & Grigorieff, N. CTFFIND4: Fast and accurate defocus estimation from electron micrographs. *J Struct Biol* **192**, 216-221 (2015). https://doi.org:10.1016/j.jsb.2015.08.008
56 Pettersen, E. F. *et al.* UCSF Chimera--a visualization system for exploratory research and analysis. *J Comput Chem* **25**, 1605-1612 (2004). https://doi.org:10.1002/jcc.20084
57 Emsley, P. & Cowtan, K. Coot: model-building tools for molecular graphics. *Acta Crystallogr D Biol Crystallogr* **60**, 2126-2132 (2004). https://doi.org:10.1107/S0907444904019158
58 Croll, T. I. ISOLDE: a physically realistic environment for model building into low-resolution electron-density maps. *Acta Crystallogr D Struct Biol* **74**, 519-530 (2018). https://doi.org:10.1107/S2059798318002425
59 Afonine, P. V. *et al.* Real-space refinement in PHENIX for cryo-EM and crystallography. *Acta Crystallogr D Struct Biol* **74**, 531-544 (2018). https://doi.org:10.1107/S2059798318006551
60 Goddard, T. D. *et al.* UCSF ChimeraX: Meeting modern challenges in visualization and analysis. *Protein Sci* **27**, 14-25 (2018). https://doi.org:10.1002/pro.3235

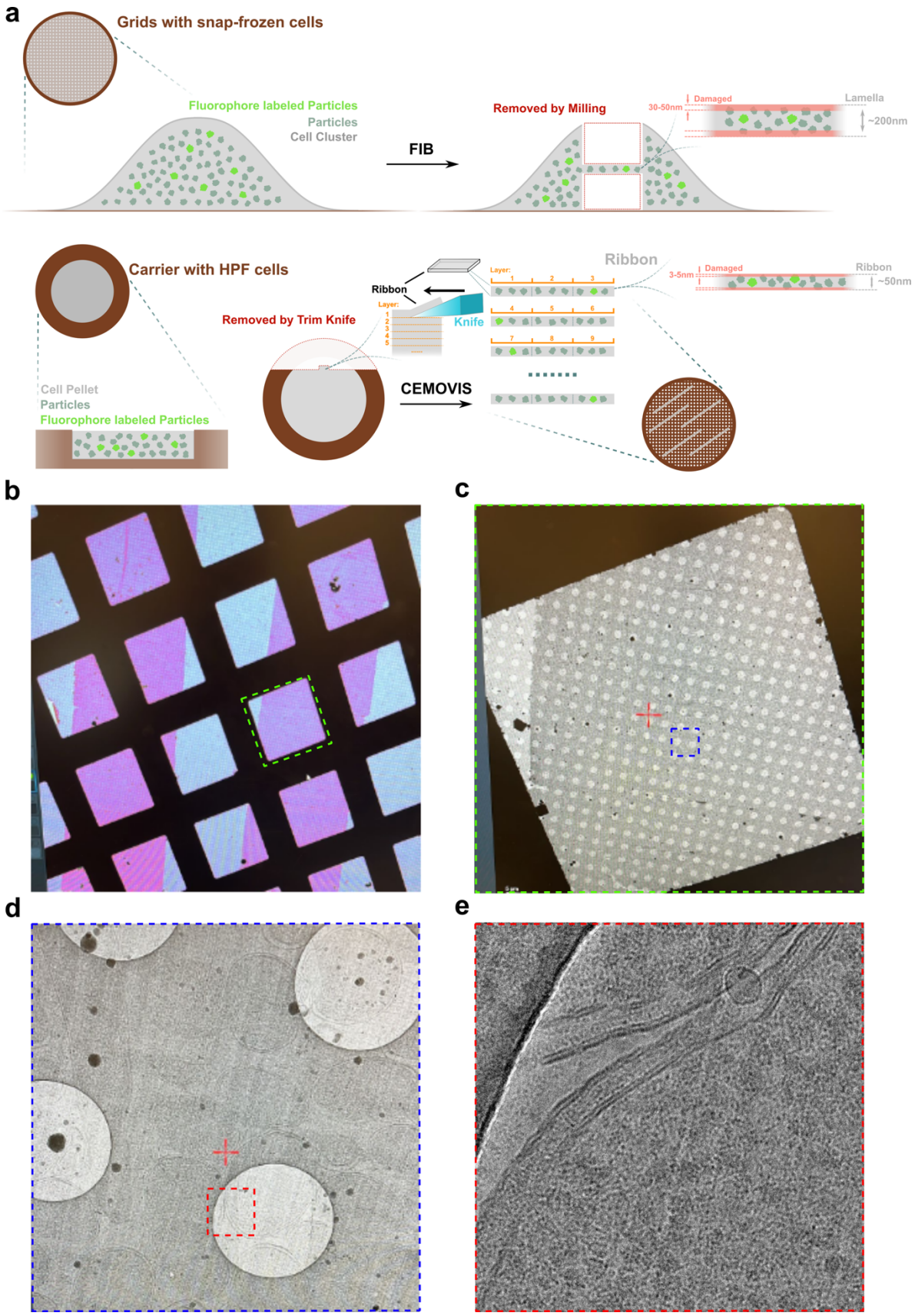
a
Grids with snap-frozen cells
Fluorophore labeled Particles
Particles
Cell Cluster
FIB
Removed by Milling
30-50nm
Damaged
Lamella
~200nm
Carrier with HPF cells
Cell Pellet
Particles
Fluorophore labeled Particles
Removed by Trim Knife
Ribbon
Layer:
Knife
CEMOVIS
Ribbon
3-5nm
Damaged
Ribbon
~50nm
b
c
d
e

**Figure 1: Using CEMOVIS to cut optimized ultrathin sections suitable for high-resolution data collection.** **a**, Comparison of FIB-SEM with CEMOVIS-produced vitreous sections. FIB lamella production irreversibly destroys the material in the *z*-direction above and below the lamella, whereas all vitreous sections in the *z*-direction remain connected, forming a ribbon that can be attached to the grid, thus avoiding the loss of potentially useful material for imaging. The surface damage in CEMOVIS is significantly less in depth compared to FIB-SEM. Fluorophore-labeled targets in CEMOVIS can be more easily detected in the *z*-direction compared to FIB-SEM. **b**, Ultrathin ribbons optimized for SPA attached to conventional Quantifoil grids. **c**, Representative image of a crevasses-free vitreous section at grid square magnification, **d**, at eucentric height magnification, and **e**, at high magnification.

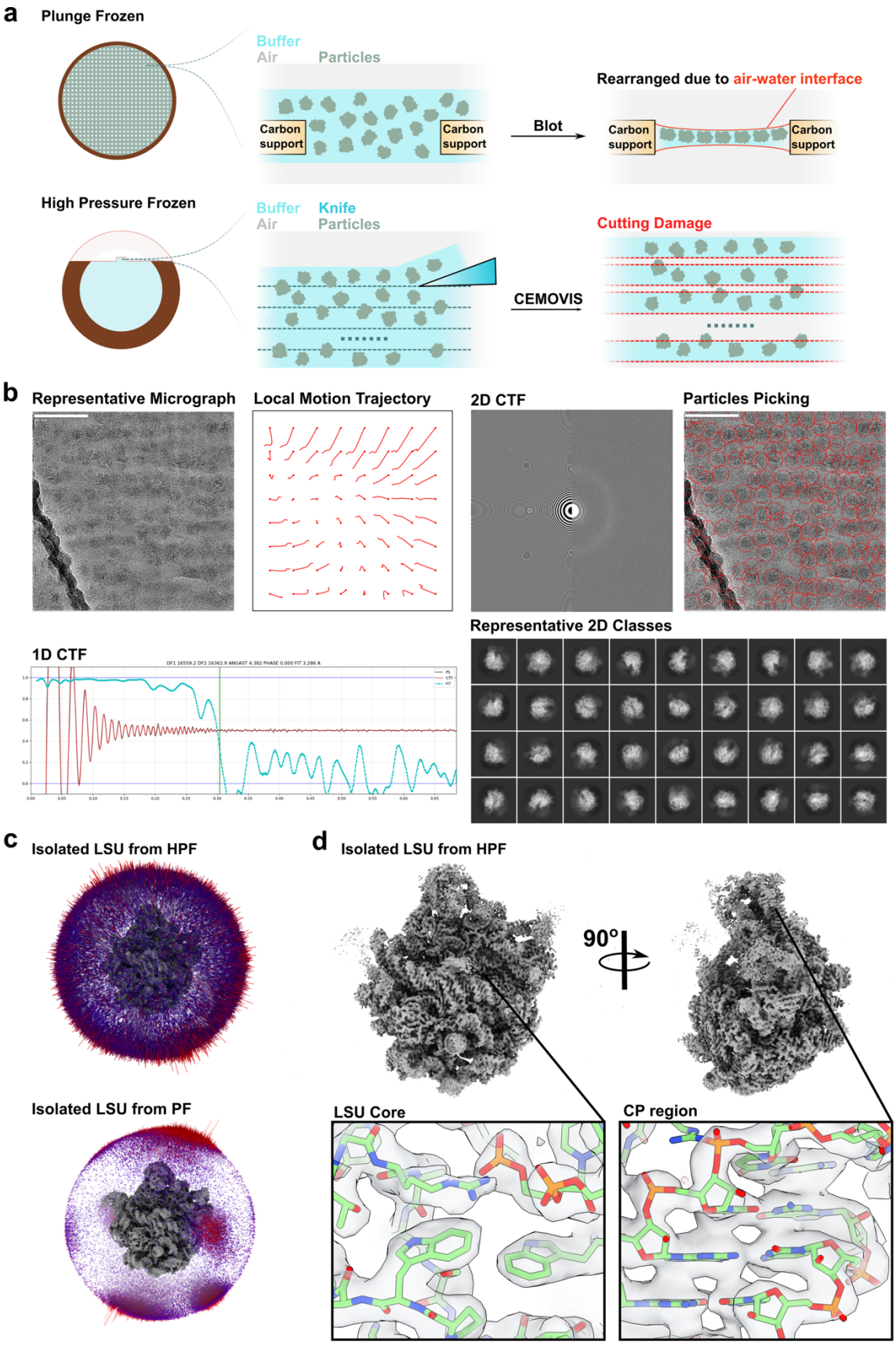
a
Plunge Frozen
Buffer
Air
Particles
Carbon support
Carbon support
Blot
Rearranged due to air-water interface
Carbon support
Carbon support
High Pressure Frozen
Buffer
Air
Knife
Particles
CEMOVIS
Cutting Damage
b
Representative Micrograph
Local Motion Trajectory
2D CTF
Particles Picking
1D CTF
Representative 2D Classes
c
Isolated LSU from HPF
Isolated LSU from PF
d
Isolated LSU from HPF
90°
LSU Core
CP region

**Figure 2: SPA of purified ribosomes at 2.75 Å from vitreous sections. a,** Grid preparation for purified proteins using conventional plunge freezing versus vitreous sections. In plunge freezing, a drop of purified protein in buffer is applied to a grid, blotted, and plunge-frozen in liquid ethane. The resulting thin layer of ice contains an air-water interface, where particles typically tend to accumulate and adopt preferred orientations. In contrast, when a high concentration of protein is frozen in a 25 µm HPF carrier, their orientation is expected to be entirely random. However, particles will be sliced during sectioning, which causes damage and results in the loss of some particles. **b,** Data collection, CTF estimation, particle picking, and 2D classification of in vitro purified ribosomes from vitreous sections. **c,** Comparison of angular distribution of ribosomes obtained from plunge-frozen grids versus vitreous sections. **d,** 2.75 Å resolution map of purified ribosomes from vitreous sections in isosurface representation. Map quality is shown in two close-up views from the LSU core and the CP region.

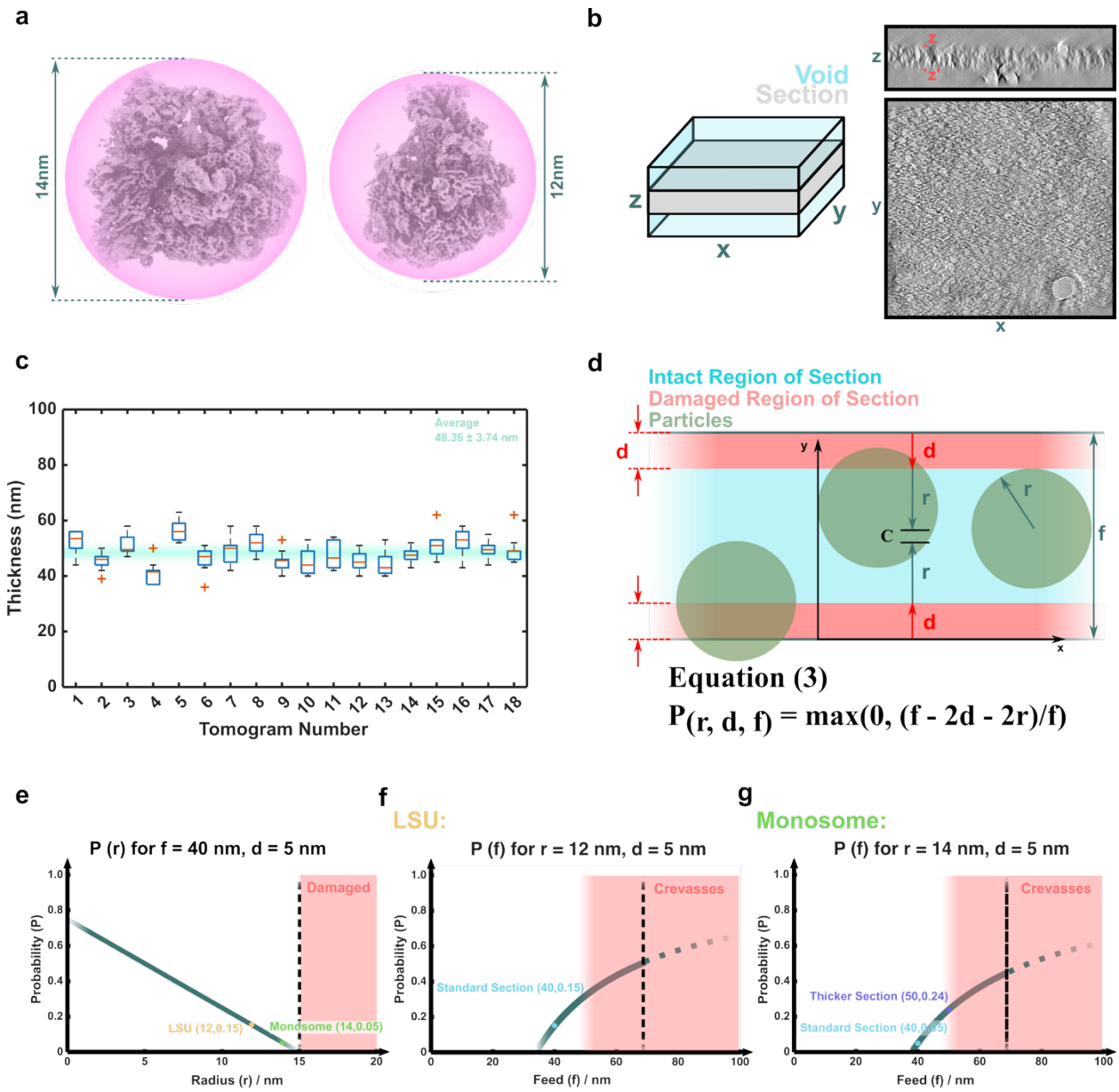


**Figure 3: Size Limitations in cryo-EM of vitreous sections. a,** Diameter of bacterial 70S and 50S ribosomal subunits. **b,** Representative tomogram of vitreous sections with indicated measurement points used for section thickness estimation. **c,** Measured thicknesses from 18 tomograms. For each tomogram, 12 locations distributed across the tomogram were sampled. The average thickness per tomogram is plotted (red line) on the y-axis. The blue box indicates the 25th and 75th percentiles. The red line shows the median values, while the black whiskers indicate the interquartile range 1.5 × (75th – 25th percentile). The red crosses show outliers outside the interquartile range. The cyan line shows the mean, blurred by the standard deviation. An overall section thickness of 48.36 ± 3.74 nm was estimated by calculating the mean of all sampling points. **d,** Simplified statistical model for particle damage in the z-direction, assuming sections are randomly sliced and proteins are randomly positioned along the z-axis. The particles are considered to be spherical. Each section has an intact region in the center and damaged regions on both sides, induced by knife marks of depth *d*. The feed thickness *f* results from the sum of the damaged and intact regions. The

probability that a particle ends up in the undamaged central part, assuming sections are sliced with a given feed thickness in z, is given by Equation (3). It is defined as the length over which the center of the sphere can be positioned without intersecting the damaged region (C), relative to the total length in which the particle can randomly end up within *f*. Note: It is assumed that the particles are spaced far apart in the x and y directions, so that overlaps do not need to be considered in this model. **e,** The function from Equation (3) is plotted as a function of protein radius, keeping f = 40 nm and d = 5 nm constant. The probability of finding an undamaged monosome is only 5% (r = 14 nm), while the probability of finding an undamaged LSU is 15% (r = 12 nm). A radius r > 15 nm will inevitably lead to particle damage, as the protein would no longer fit within the 30 nm undamaged zone. **f–g,** Equation (3) is plotted with constants r = 12 nm (LSU) or r = 14 nm (monosome) and d = 5 nm, and with *f* as the variable. With increasing section thickness, the probability of finding an intact LSU increases. However, at thicknesses greater than 50 nm, crevasses begin to appear due to the cutting process, which can damage particles and result in suboptimal sections for imaging (dark areas). Sections thicker than 70 nm will inevitably suffer from crevasses.

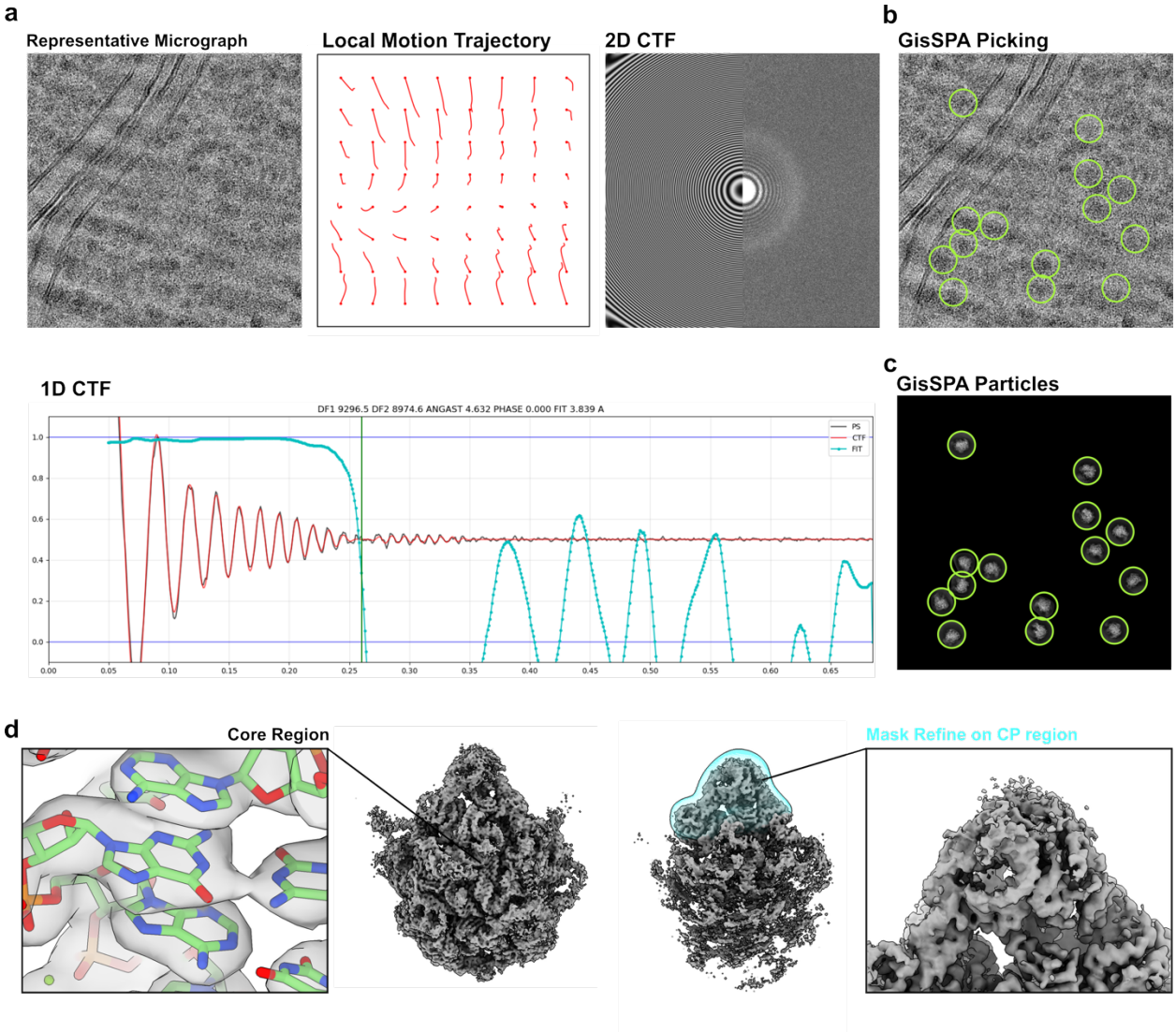


**Figure 4: *In situ* cryo-EM structure of the bacterial 50S ribosomal subunit at 2.98 Å resolution from vitreous sections. a,** Representative motion-corrected micrograph with local motion trajectories and the 2D, and 1D CTF fits are shown. **b,** 2D template matching (2DTM) using GisSPSA software with the plunge-frozen 3D reference volume of the 50S subunit as the search model. **c,** Corresponding hits from panel b shown without background noise from the cellular environment. **d,** High-resolution map showing side-chain details of the 50S ribosomal subunit, along with a CP-focused refined map demonstrating the internal intactness of the CP region.